ROYAL SOCIETY OF CHEMISTRY

PAPER

Check for updates

Enhanced phase transition and infrared photoresponse characteristics in VO$_2$(M1) thin films synthesized by DC reactive sputtering on different substrates

Inyalot Jude Tadeo, [ID] * Saluru B. Krupanidhi and Arun M. Umarji [ID]

VO$_2$ is a material with high potential for low-cost optoelectronic, switching and energy saving devices. This work presents the synthesis of smooth high-quality VO$_2$(M1) thin films on quartz (VO$_2$-Qu) and c-sapphire (VO$_2$-Saph) substrates by two-step DC reactive sputtering with enhanced semiconductor-to-metal transition (SMT) and infrared (IR) photoresponse characteristics. Phase formation and purity were confirmed by XRD and Raman measurements. Morphological analysis by AFM and SEM revealed the nanosized nature of the films with a surface roughness of 37 $\pm$ 0.5 nm and 48 $\pm$ 1 nm for VO$_2$-Qu and VO$_2$-Saph thin films respectively. The VO$_2$-Qu and VO$_2$-Saph thin films exhibit thermally activated SMT temperature (T_{SMT}) of 71 °C and 68 °C with resistance change of 4 and 5 orders of magnitude respectively. Infrared (λ = 1064 nm and 1550 nm) photoresponse characteristics of the low-cost photodetector fabricated based on the synthesized VO$_2$(M1) films increase with a decrease in film roughness. The responsivity increases in the order VO$_2$-Qu (14.02 mA W^{-1}) > VO$_2$-Saph (11.1$_2$ mA W^{-1}) under an IR (λ = 1064 nm, 250 mW cm^{-2}) laser at a bias voltage of 10 V. The higher energy (λ = 1064 nm) laser yields an enhanced photoresponse compared to the lower energy (λ = 1550 nm) laser owing to the efficient generation of charge carriers with a higher laser energy. This work provides a way for the large-scale synthesis of high-quality VO$_2$(M1) thin films for various device applications.

1. Introduction

Vanadium dioxide (VO$_2$) is a narrow bandgap (0.6–1.0 eV) n-type phase change material[1–6] and is widely studied due to its ability to undergo reversible 1st order semiconductor to metal transition at $\sim$68 °C, usually accompanied by a drastic resistance change of 3–5 orders of magnitude.[3,7–10] This is followed by a change in its optical, transport, magnetic and electrical properties.[11,12] These exciting properties make VO$_2$ an appealing material for application in many switching devices like smart windows,[13–15] field-effect transistors (FETs),[11,16] micro-bolometers,[17] thermal rectifiers[18] and actuators[19] due to the extremely fast switching time, as little as 100 femtoseconds.[20,21] In technological advancement, phase change materials[22–24] and photodetectors play a key role in several optoelectronic devices as they facilitate the conversion of light of different wavelengths into electric signals. IR photodetectors are of great importance to many sectors ranging from civilian to military.[25] Photodetectors have large market value emanating from their numerous applications, including remote sensing, thermography, high-resolution imaging, environmental monitoring, astronomy, industrial processing control, scientific

research, military, security checks, night vision cameras, light-wave communication and optoelectronic circuits.[25–27] To develop high quality optical and electronic thin film devices based on VO$_2$, the phase must be stabilized, surface roughness should be reduced, and a jump in resistance of at least 3 orders of magnitude must be attained in the films. Monoclinic (M1) VO$_2$ thin films synthesized by numerous single-step and two-step techniques like chemical vapor deposition,[28] DC reactive sputtering[29] and ultrasonic nebulized spray pyrolysis of aqueous combustion mixtures[30] have been shown as low-cost infrared photodetectors. However, the roughness and infrared photoresponse performance of the thin films vary with the substrate's nature and the deposition technique.[28–31] Thus, it is vital to understand the crystallization behavior and infrared photoresponse characteristics of VO$_2$(M1) thin films synthesized on different substrates to elucidate the phase formation to improve the quality of films for various device applications. Numerous other techniques like pulsed laser deposition,[32] sol–gel,[33] atomic layer deposition,[34] atmospheric pressure chemical vapor deposition,[35] spray pyrolysis,[36–38] spin-coating,[39] metal–organic chemical vapor deposition,[40] molecular beam epitaxy,[41] and hydrothermal[42] and electron beam evaporation[43] have been used to synthesize thin films of VO$_2$ exhibiting a resistance change of 3–5 orders of magnitude on different substrates for

Materials Research Centre, Indian Institute of Science, Bengaluru, 560012, Karnataka, India. E-mail: inyalottadeo@iisc.ac.in

various applications. Most switching applications require functional SMT materials like VO$_2$ that show a large resistance drop, sharp hysteresis loop and large transition contrast.[44,45] However, phase inhomogeneity and interfacial mismatch between the substrate and the active material greatly hinder their application by rendering reduced transition strength, large hysteresis and low transition contrast, which are profoundly shown to be dependent on the substrate and other thin film deposition parameters.[45] Of late, an enormous amount of research has been geared towards improving the crystallinity and stoichiometry of functional materials where the thin film deposition parameters like temperature, pressure and substrate nature are investigated.[6,45] The choice of substrate depends on cost and target application. For instance, Si-based substrates like Si(100), PtSi, p-Si and n-Si are employed in FET based industries while non-Si substrates like glass, quartz, and sapphire are used in thermal and optical devices.[2,3,46,47] The sapphire substrate is known to yield polycrystalline VO$_2$ films exhibiting a change in resistance of 4–5 orders of magnitude.[2,46,47] Thus, a thorough understanding of the effect of the substrate is greatly desired for effective use of VO$_2$ thin films in various devices.

Herein, smooth, high-quality VO$_2$(M1) films were synthesized on quartz and c-sapphire substrates by two-step DC reactive sputtering. DC reactive sputtering is a robust technique that yields large-area high-quality, smooth thin films on a large-scale with specific stoichiometry for several device applications.[29,48,49] The choice of substrates was based on their structural and physical properties. Quartz is an amorphous substrate and has low thermal conductivity which is particularly useful for high temperature applications. Sapphire has high thermal conductivity which allows quick switching of the deposited films, which is useful for pixel-based applications.[2,46,47] Also, the transparent nature of quartz and sapphire substrates makes them useful in various optical industries. The two-step synthesis technique was employed due to the challenges in the synthesis of single-phase VO$_2$ thin films[29,31] coupled with the effectiveness of our well established reduction technique reported elsewhere,[50] in yielding high-quality VO$_2$(M1) thin films. The influence of the substrate on the SMT and IR photoresponse properties of the synthesized VO$_2$(M1) thin films was investigated where it had a profound effect on the structure, SMT and IR photoresponse characteristics of the films.

2. Experimental

2.1. Synthesis

The VO$_2$(M1) thin films were achieved in a two-step process. In the first step, V$_2$O$_5$ thin films were synthesized on quartz and c-sapphire substrates by a DC reactive sputtering (Hydro Pneo Vac Technologies) unit using deposition conditions specified in Table 1. All the substrates were placed on the heater plate at the same time and equilibrated for 30 minutes to ensure uniform deposition temperature. It is assumed that the temperature measured at the heater base plate is in equilibrium with surface temperatures of the different substrates. The base chamber pressure was attained before commencing the deposition process. The working pressure was kept constant throughout the deposition time. Reactant gases consisting of oxygen and argon

Table 1 Parameters used for depositing V$_2$O$_5$ thin films by DC reactive sputtering

Parameter	Value
Target	V metal (2″ × 0.25″, 99.99% pure)
Substrate	Quartz and c-sapphire
Distance between the target and substrate	10 cm
Base chamber pressure	5.3×10^{-5} mbar
Working pressure	8.1×10^{-3} mbar
Power	200 W
Argon flow rate	5 sccm
Oxygen flow rate	0.05 sccm
Deposition temperature	450 °C
Duration of deposition	45 minutes

were maintained at a flow rate of 0.05 and 5 sccm respectively, using MKS mass flow controllers. Pre-sputtering was done for 15 minutes to remove any contamination on the target material before the deposition of thin films commenced, which was performed in a 0.095 m^3 chamber at a substrate temperature of 450 °C for 45 minutes. This gave phase pure V$_2$O$_5$ thin films.

The second step involved a controlled reduction of synthesized V$_2$O$_5$ films to give VO$_2$(M1) films using our well established reduction technique.[50] A schematic diagram of the in-house built reduction setup is given in Fig. 1. Briefly, the sample is placed in a quartz tube with one of its ends closed and kept in a tubular furnace. The other end of the tube is attached to a specially designed coupler which is used to connect it to a bubbler containing a hydrocarbon like *n*-hexane, benzene or toluene. The bubbler is in turn connected to a nitrogen gas cylinder through the mass flow controller (MKS Instruments, USA) which is used to control the flow rate as the gas saturates with the hydrocarbon. N$_2$ gas, saturated with the hydrocarbon, was continuously flowed into the furnace at a rate of 45 sccm. The as synthesized V$_2$O$_5$ thin films were kept in the reduction chamber at 550 °C for 2 hours and then cooled to room temperature giving phase pure VO$_2$ thin films.

The V–O phase diagram,[8,51] specifically the correlation between the partial pressure of oxygen, temperature and the phase stability were used to deduce optimum conditions for reduction so
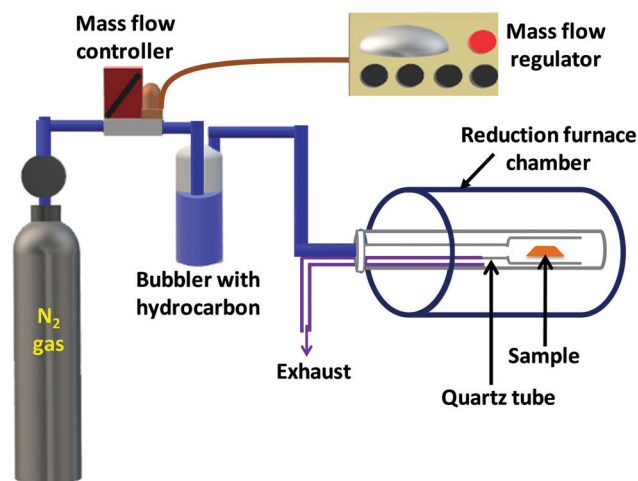

Fig. 1 Schematic diagram of the in-house built setup used to reduce V$_2$O$_5$ thin films into VO$_2$ thin films.

Table 2 Sample codes used to represent the synthesized V_2O_5 and $VO_2(M1)$ thin films

Sample code (V_2O_5 based)	Sample code (VO_2 based)	Substrate
V_2O_5-Qu	VO_2-Qu	Quartz
V_2O_5-Saph	VO_2-Saph	c-Sapphire

that single phase VO_2 would result. The synthesized thin films were represented by sample codes as given in Table 2.

2.2. Characterization

Phase purity was analyzed from X-ray diffraction measurements carried out using a PANalytical instrument with Cu Kα radiation (1.5418 Å) at a scan rate of $2°$ min^{-1}. Phase formation and its purity were confirmed from Raman measurements recorded using the Horiba JobinYvon HR-Raman-123 microPL spectrometer at a wavelength of 532 nm. The thin film morphology was investigated using a non-contact mode A.P.E. Research A100-AFM atomic force microscope and an Inspect F50 field emission scanning electron microscope. The Veeco Dektak 6M surface profilometer was used to measure the thickness of thin films. SMT characteristics of $VO_2(M1)$ thin films were studied from electrical measurements performed using a DC electrical probe station equipped with the ATT thermal controller and coupled with a B1500A semiconductor device analyzer.

2.3. Fabrication of a photodetector device

The IR photodetector devices used for the photodetection studies were fabricated by depositing electrical contacts comprising of Cr (6 nm)/Au (80 nm) and measuring 1 mm × 1 mm in width and length on top of the synthesized VO_2 thin films by thermal evaporation aided by a mask. The photoresponse properties of devices were recorded using a Keithley SMU2400 source meter. A CNI MDL-III 1550 nm laser with an optical coupler of ~2 mm and an MIL-III 1064 nm laser (beam radius of 2.5 mm) were used as the infrared source.

3. Results and discussion

3.1. Structural characterization: XRD studies

Fig. 2a presents the XRD patterns of V_2O_5-Qu and V_2O_5-Saph thin films deposited by DC reactive sputtering. The synthesized

V_2O_5-Qu and V_2O_5-Saph thin films were then reduced to give VO_2-Qu and VO_2-Saph thin films respectively, whose phase formation and purity were confirmed from their XRD patterns shown in Fig. 2b.

All thin films deposited were phase pure as no impurity peak of other vanadium oxides was detected. The V_2O_5 was indexed to the *Pmmn* space group of the orthorhombic crystal system (JCPDS #77-2418),[52,53] and VO_2 was indexed to the monoclinic (M1) phase of VO_2 with the space group $P2_1/c$ (JCPDS #82-0661).[28–31,54] Achieving the right conditions for thin film deposition and reduction, most especially temperature, oxygen partial pressure and using a nitrogen atmosphere saturated with hydrocarbons to yield the desired $VO_2(M1)$ films is one of the greatest accomplishments of this study.

3.2. Raman spectroscopy studies

The phase formation and purity of the synthesized $VO_2(M1)$ thin films were further confirmed from room temperature Raman measurements. Fig. 3a shows the room temperature Raman spectra of V_2O_5-Qu and V_2O_5-Saph thin films deposited by DC reactive sputtering. All the V_2O_5-Qu and V_2O_5-Saph thin films featured 10 Raman peaks at peak positions matching those reported for crystalline V_2O_5.[53,55–59] The Raman peaks observed were assigned to various bending and stretching vibrational modes of V_2O_5 as $102(A_g)$, $145(B_{2g}, B_{3g})$, $197(B_{1g})$, $283(B_{3g}, B_{2g})$, $304(A_g)$, $404(A_g)$, $487(A_g)$, $528(A_g)$, $703(B_{3g}, B_{2g})$ and $995(A_g)$ cm^{-1}.[53]

Fig. 3b shows the Raman spectra, taken at room temperature, for VO_2-Qu and VO_2-Saph thin films synthesized by two-step DC reactive sputtering. The Raman spectra of VO_2-Qu and VO_2-Saph thin films showed 11 distinct peaks corresponding to monoclinic (M1) VO_2[16,28–31,60,61] further proving the phase purity of the synthesized thin films. The peaks were observed at positions 142, 193, 223, 261, 308, 338, 387, 442, 499, 614 and 822 cm^{-1} and were assigned to the phonon modes B_{1g}, A_g, A_g, A_g, A_g, A_g, A_g, E_g, A_g, A_g and B_{2g} respectively, of $VO_2(M1)$.[16,62]

3.3. Morphological analysis

The surface morphology of the deposited $VO_2(M1)$ thin films was investigated using AFM and SEM. Fig. 4 shows 3D AFM images of VO_2-Qu and VO_2-Saph thin films deposited by two-step DC reactive sputtering. They clearly show the smooth
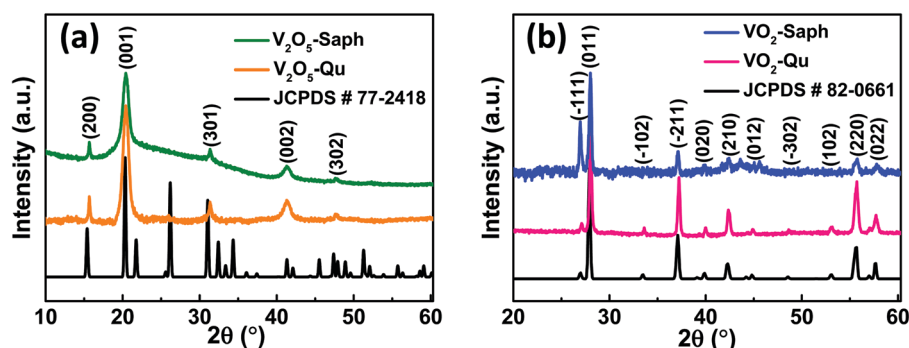

Fig. 2 XRD patterns of (a) V_2O_5-Qu and V_2O_5-Saph thin films; and (b) VO_2-Qu and VO_2-Saph thin films deposited by DC reactive sputtering.
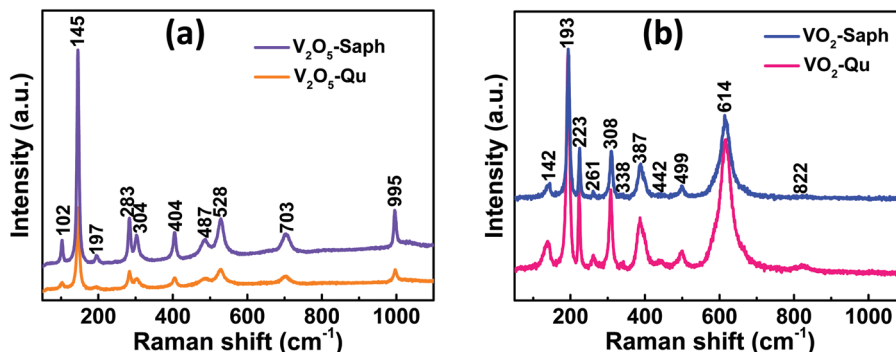
Fig. 3 Room temperature Raman spectra of (a) V_2O_5-Qu and V_2O_5-Saph thin films; and (b) VO_2-Qu and VO_2-Saph thin films deposited by DC reactive sputtering.
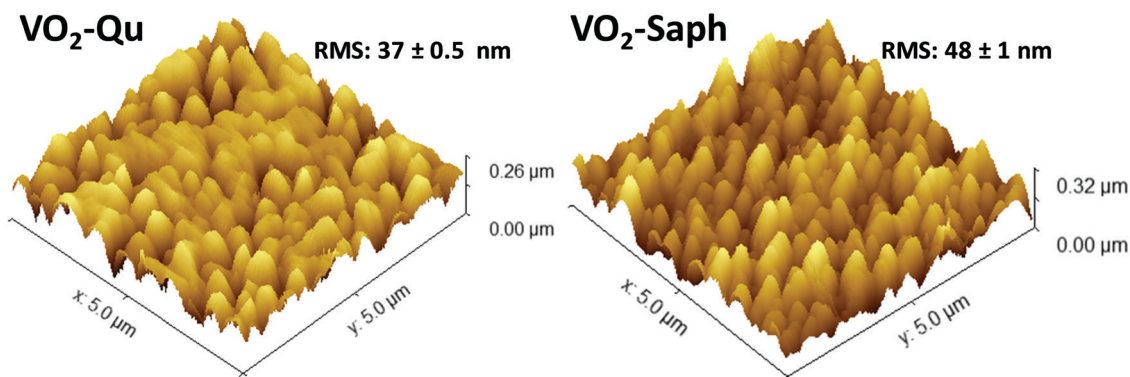

Fig. 4 3D AFM images of VO_2-Qu and VO_2-Saph thin films synthesized by two-step DC reactive sputtering.

nature of the thin films having well-grown and uniform grains. The VO_2-Qu and VO_2-Saph thin films deposited by two-step DC reactive sputtering had relatively low surface roughness of 37 ± 0.5 and 48 ± 1 nm respectively, justifying their suitability for use in several optical devices as they scatter light to a lesser extent.

The thickness of the deposited VO_2(M1) thin films was 150–160 nm from Veeco Dektak 6M surface profilometer measurements.

Fig. 5 shows SEM images of VO_2-Qu and VO_2-Saph thin films synthesized by two-step DC reactive sputtering. They clearly show the well-grown grains, packed and continuous, suitable for application in various optoelectronic and switching devices. The substrate effect is visible on the shape, size and compactness of grains, with VO_2-Saph thin films showing the most compact
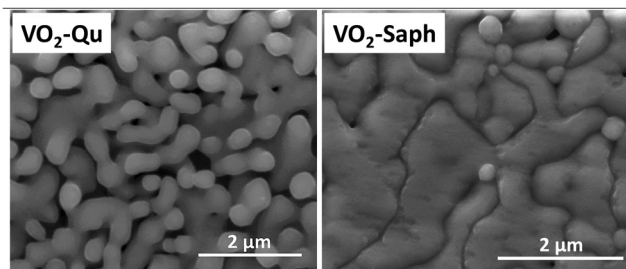
and largest particle size. The average particle size, determined using Image-J software[63] was 155 ± 7 nm and 260 ± 4 nm for VO_2-Qu and VO_2-Saph thin films respectively.

3.4. Electrical studies

The electrical properties were analysed from I–V measurements recorded on VO_2-Qu and VO_2-Saph thin films as a function of temperature (25 °C to 110 °C). The resistance (R) obtained from the slope of voltage *versus* the current plot was then plotted against temperature. Fig. 6(a and c) show plots of normalized resistance ($R(T)/R(RT)$) *versus* temperature for VO_2-Qu and VO_2-Saph thin films respectively. The dependence of resistivity of VO_2 thin films on the temperature is an indication of SMT and the magnitude of resistance change shows the quality of the thin films. The VO_2-Qu and VO_2-Saph thin films exhibited an abrupt first-order SMT with a change in resistance of 4 and 5 orders of magnitude respectively. The highest resistance change (5 orders of magnitude switching) exhibited by VO_2-Saph thin films is comparable to that shown by single crystals[64] of VO_2 and it indicates complete growth of thin films with good connectivity.[2,47]

Fig. 6(b and d) show the derivative plots for VO_2-Qu and VO_2-Saph thin films from which the SMT temperatures (T_{SMT}) were obtained. The T_{SMT} was observed not to happen at a single temperature as different peaks were identified during heating and cooling cycles. The VO_2-Qu and VO_2-Saph thin films exhibited thermally activated T_{SMT} of 71 °C and 68 °C, respectively, which

Fig. 5 SEM images of VO_2-Qu and VO_2-Saph thin films deposited by two-step DC reactive sputtering.
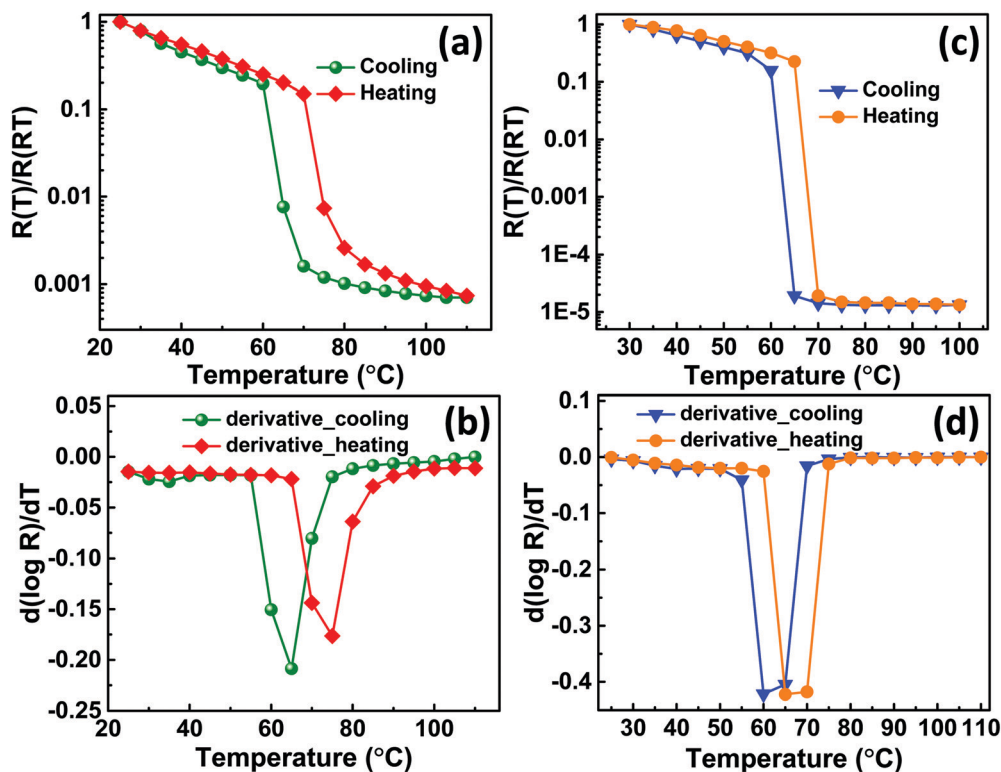
Fig. 6 (a and c) Normalized resistance as a function of temperature plots for VO$_2$-Qu and VO$_2$-Saph thin films respectively; (b and d) heating and cooling derivative d(log R)/dT plots for VO$_2$-Qu and VO$_2$-Saph thin films respectively, deposited by two-step DC reactive sputtering.

was in agreement with other reports.[3,10,47] The resistance ratio (ΔA), expressed as $\Delta A = \dfrac{R(T_1)}{R(T_m)}$, indicates the strength of the transition where $R(T_1)$, $R(T)$ and $R(T_m)$ denote the resistance at initial/room temperature (T_1/RT), any temperature (T), and maximum/final temperature (T_m) respectively. The resistance ratio (ΔA), transition width (ΔT), thermal hysteresis (ΔT_h) and the temperature coefficient of resistance (TCR), which measures the change in resistance of a material per degree of temperature change, were determined as given in Table 3.

The VO$_2$-Saph thin films exhibited the highest switching ratio and the lowest hysteresis width, which are desirable for

fabricating high-quality devices used for various switching applications. It's clear from Table 3 that the synthesized VO$_2$-Qu and VO$_2$-Saph thin films exhibit better SMT characteristics than VO$_2$(M1) films deposited on Si(100) substrate by the same deposition technique.[29] The high values of resistance ratio shown by all thin films are attributed to the complete formation of the monoclinic (M1) phase of VO$_2$ with no other phase.[28–31] No appreciable change in the TCR values was observed for all the films; the recorded values were consistent with the literature reports.[65,66] The activation energies, E_a of VO$_2$-Qu and VO$_2$-Saph thin films were determined from the relation $R(T) = R_0\,e^{E_a/k_B T}$ where E_a is the slope of $\ln R(T)$ *versus* $1/k_B T$ plot.[29–31] The activation energies of the deposited VO$_2$(M1) thin films were determined for both heating and cooling curves as shown in Fig. 7. The VO$_2$-Saph thin films showed the highest (5 orders of magnitude) change in resistance and exhibited the lowest activation energies in the high-temperature phase.

Also, it has the maximum change in E_a on switching, indicating that the high-temperature phase is almost entirely metallic with a sapphire substrate. VO$_2$ in the 'metallic' phase is considered a 'poor metal'.[67–69] Also, the 'metallic' phase might not be ideally metallic because of the presence of defects due to the deposition technique and conditions.[69]

3.5. Photodetection studies

The photoresponse characteristics of the fabricated photo-detector devices based on the synthesized VO$_2$(M1) thin films were investigated by shining an infrared laser (λ = 1064 nm and

Table 3 Comparison of SMT properties from electrical measurements of VO$_2$-Qu and VO$_2$-Saph thin films synthesized by two-step DC reactive sputtering with those of VO$_2$(M1) thin films deposited on the Si(100) substrate (VO$_2$–Si(100)) by the same technique

| Sample	VO$_2$-Qu	VO$_2$-Saph	VO$_2$–Si(100)[29]
Surface roughness (nm)	37 ± 0.5	48 ± 1	8 ± 0.7
Transition temperature, T_c (°C)	71	68	68
Transition width, ΔT (°C)	9	5	10
Thermal hysteresis, ΔT_h (°C)	10	5	10
Resistance ratio, ΔA on heating	1356	75 187	164
Resistance ratio, ΔA on cooling	1425	75 216	181
TCR at 30 °C (% K^{-1}) on heating	−1.25	−1.25	−1.24
TCR at 30 °C (% K^{-1}) on cooling	−1.25	−1.25	−1.24
E_a (± error) (meV) on heating	364 ± 11	336 ± 22	228 ± 12
	318 ± 3	48 ± 6	198 ± 16
E_a (± error) (meV) on cooling	128 ± 15	21 ± 11	119 ± 7
	370 ± 4	399 ± 10	361 ± 56
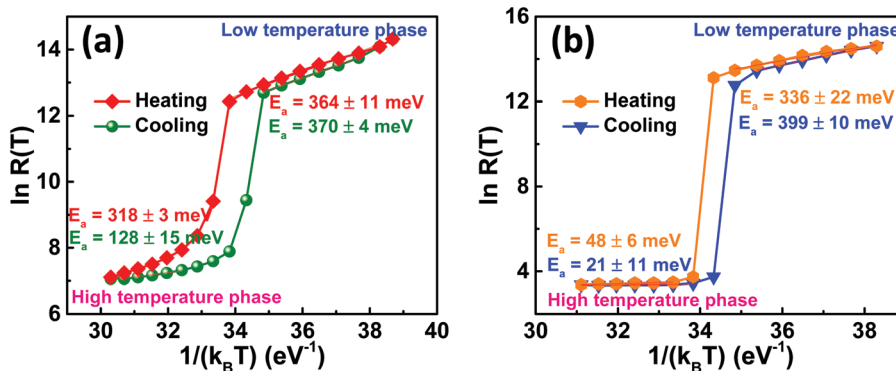
Fig. 7 Activation energy studies from $\ln R(T)$ against $1/k_B T$ plot during heating and cooling cycles for (a) VO$_2$-Qu and (b) VO$_2$-Saph thin films synthesized by two-step DC reactive sputtering.

1550 nm) under different power densities at room temperature. The schematic diagram of the fabricated device is presented in Fig. 8a. Fig. 8b shows room temperature $I–V$ curves in the dark and on illuminating with a 1064 nm laser at different intensities for photodetector fabricated based on VO$_2$-Qu thin films. The curves were linear, signifying the ohmic nature of contacts. VO$_2$-Saph thin films exhibited similar $I–V$ curves.

Fig. 9(a–d) shows the change in photocurrent with respect to time for the photodetector fabricated based on (a and b) VO$_2$-Qu and (c and d) VO$_2$-Saph thin films upon illumination with (a and c) 1064 nm laser and (b and d) 1550 nm laser under constant power density of 250 mW cm^{-2} at a bias voltage of 5 V and 10 V. The photoresponse increased with the increase in bias voltage, an observation consistent with the power law.[70]

The increase in photocurrent is attributed to the efficient separation of charge carriers with fewer trap states and interaction between photogenerated carriers at higher bias. At lower bias trap states, the interactions between the photogenerated carriers (electron–hole pairs) are involved in the recombination kinetics of photocarriers which leads to a low photocurrent.[70,71] The photoresponse was repeated for many cycles but only a few cycles are given to avoid clutter. The photocurrent, given in Fig. 10a, was observed to increase with a reduction in the thin film surface roughness under both cases of laser energies. The

photocurrent increased in the order: VO$_2$-Qu (8.59–27.55 μA) > VO$_2$-Saph (3.03–21.85 μA) while the surface roughness varied as VO$_2$-Qu (RMS: 37 ± 0.5 nm) < VO$_2$-Saph (RMS: 48 ± 1 nm). This trend in photoresponse exhibited by the synthesized thin films can be ascribed to the effect of light scattering, which reduces with a reduction in the surface roughness of thin films. The responsivity indicates how the efficiency of a detector responds to the optical signal.[72] R_λ is defined as photocurrent realized per unit power of incident light on the effective area of the device and expressed as $R_\lambda = \dfrac{I_{ph}}{P_\lambda A}$; where I_{ph} is photocurrent $I_{ph} = I_{light} - I_{dark}$, P_λ is power density and A is the effective area of the device.[71,72] EQE is a ratio of the number of electron–hole pairs (n_e) with a contribution to the photocurrent to the total number of incident photons ($n_{photons}$). It is defined as a measure of the number of photons absorbed to the number of incident photons and expressed as $EQE = \dfrac{n_e}{n_{photons}} = \dfrac{hcR_\lambda}{q\lambda}$; where h is Planck's constant, c is the speed of light, q is the electron charge and λ is the wavelength of the laser used.[70,71] Detectivity determines the sensibility of a device to detect weak optical signals and is calculated from the relation $D^* = \dfrac{I_{ph}}{P_\lambda (2qI_{dark}A)^{1/2}} = \dfrac{R_\lambda A^{1/2}}{(2qI_{dark})^{1/2}}$;
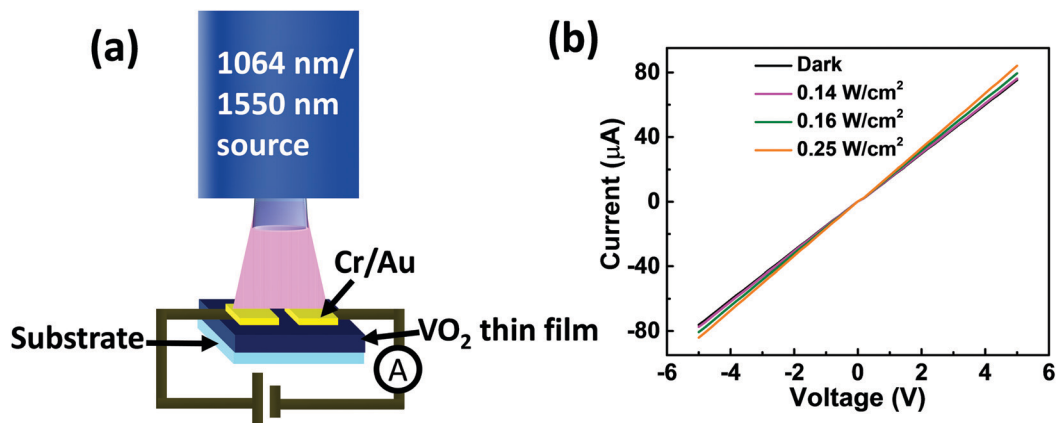

Fig. 8 (a) Device schematic and (b) $I–V$ curves for the device fabricated based on VO$_2$-Qu thin films in the dark and on illuminating with infrared (1064 nm) laser at different power densities.
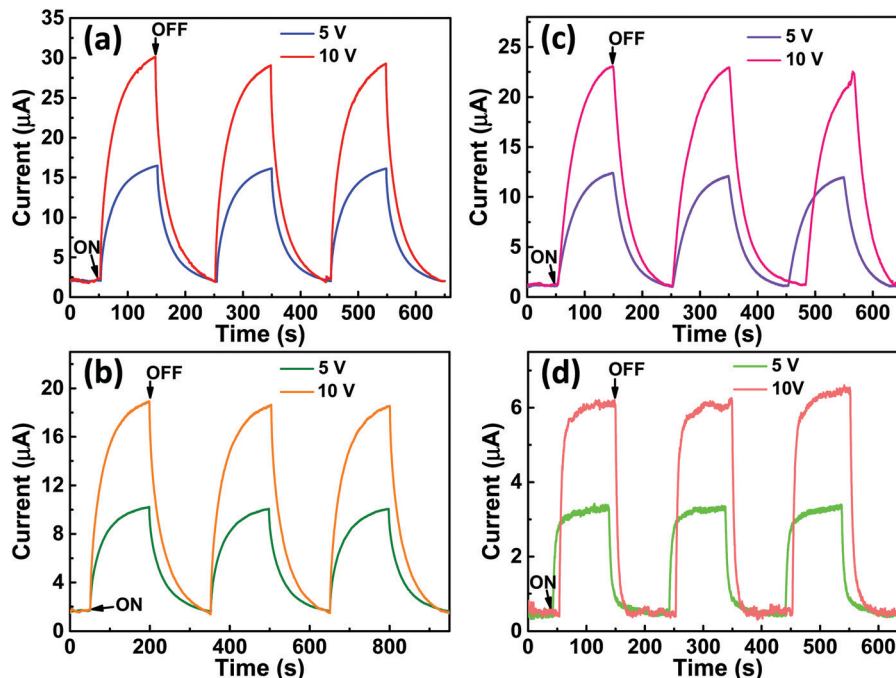
Fig. 9 ON and OFF photoresponse characteristics of the fabricated device based on (a and b) VO$_2$-Qu and (c and d) VO$_2$-Saph thin films deposited by two-step DC reactive sputtering upon illumination with a (a and c) 1064 nm laser and (b and d) 1550 nm laser under constant power density of 250 mW cm^{-2} at 5 V and 10 V bias voltage.

where A, the effective area of detector, is in cm^2.[71,73] A high detectivity indicates a better performance of the photodetector.

Fig. 10(b–f) show responsivity, quantum efficiency, detectivity, response time and retrace time respectively, of the photodetector fabricated based on VO$_2$-Qu and VO$_2$-Saph thin films upon illumination with an IR (λ = 1064 nm and 1550 nm) laser with a power density of 250 mW cm^{-2} at 5 V and 10 V bias. In all thin films, the infrared photoresponse of the photodetector decreased
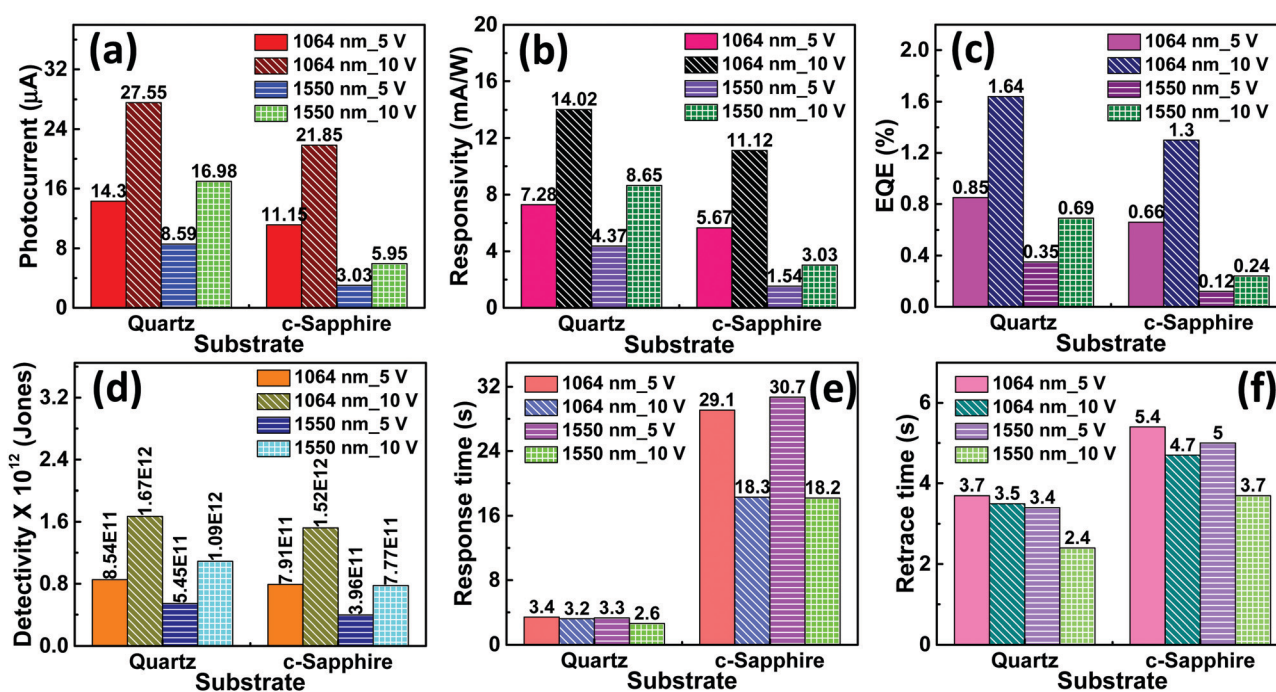

Fig. 10 Comparison of photoresponse properties of the photodetector fabricated based on VO$_2$-Qu and VO$_2$-Saph thin films synthesized by two-step DC reactive sputtering under illumination with IR (λ = 1064 nm and 1550 nm) laser in a constant power density of 250 mW cm^{-2} at a bias voltage of 5 V and 10 V; (a) photocurrent, (b) responsivity, (c) EQE, (d) detectivity, (e) response time and (f) retrace time.

Table 4 The performance of our photodetector devices compared with reported IR photodetectors

IR photodetector	R_λ (mA W^{-1}) at λ (nm)		$D^\star$ (jones) at λ (nm)		τ_{resp} (s)	τ_{retr} (s)
	1064	1550	1064	1550		
VO$_2$(M1) thin films[30]	1.54		3.53×10^{10}		1.17	1.08
SnS$_2$ thin films[71]	1.8		10^{11}		2.5	3.68
WS$_2$ monolayer[70]	6.6				0.004	0.005
VO$_2$(M1) thin films[28]		7.13×10^{-2}		1.06×10^{11}	2.23	3.67
VO$_2$(M1) thin films[29]	40.1		3.0×10^{12}		0.1–0.14	0.1–1.2
P3HT–PCBM polymer[75]		3.01		7.97×10^8	4.9	6.3
This work						
VO$_2$-Qu thin films	14.02	8.65	1.67×10^{12}	1.09×10^{12}	2.5–3.2	2.4–3.5
VO$_2$-Saph thin films	11.12	3.03	1.52×10^{12}	7.77×10^{11}	18.2–18.3	3.7–4.7

R_λ is responsivity, $D^\star$ is detectivity, τ_{resp} is response time and τ_{retr} is retrace time.

with an increase in the surface roughness of the thin films, which can be ascribed to the effect of increased light scattering arising from the increased surface roughness of the thin films.[74] The performance of our photodetector devices are compared with previously reported infrared photodetector devices in Table 4.[28,30,70,71,75] The responsivity and the detectivity exhibited by our devices at both laser energies (λ = 1064 nm and 1550 nm) are better than those reported.[28,30,70,71,75]

The dynamic response of the fabricated device to IR source can be described by exponential equations $I(t)_{growth} = I_{dark} + \alpha e^{t/\tau_1} + \beta e^{t/\tau_2}$ and $I(t)_{decay} = I_{dark} + \chi e^{-t/\tau_1} + \gamma e^{-t/\tau_2}$ for growth and decay respectively,[71,76,77] where t is time for ON or OFF cycles; I_{dark} is dark current, τ_1 and τ_2 are time constants; α, β, χ and γ are the scaling constants. The response and the retrace time were determined from the solutions to those 2nd order exponential equations by fitting one cycle of each of the growth and decay response curves, at 5 V and 10 V. The average response time constants were then computed from the relation $\tau_{average} = \dfrac{(\alpha\tau_1 + \beta\tau_2)}{\alpha + \beta}$.[71] The response time and retrace time exhibited by our devices were comparable to those reported. The mechanism of photodetection is based on the principle of the photovoltaic effect. It involves the generation of excess free electron–hole pairs (charge carriers) by a material absorbing photons with photon energy greater than the material's bandgap which leads to a reduction in its electrical resistance.[78] Before the application of bias, charge carriers present in VO$_2$(M1) thin films are free. On application of an external bias, the barrier is overcome, charge carriers go to respective electrodes contributing to the dark current and the metal-semiconductor interface gets depleted of charge carriers. On illuminating the photodetector device fabricated based on the synthesized VO$_2$(M1) thin films with the photon energy of λ = 1064 nm or 1550 nm $\sim$1.16 eV or 0.8 eV respectively, which is greater than the bandgap of VO$_2$ (0.6–0.7 eV),[3,79] the VO$_2$(M1) thin film absorbs the radiation, charge carriers (excitons) are generated and separated by applied bias. These carriers collect at the electrodes and add to the available dark current making up the recorded photocurrent.[78] To rule out the substrate's contribution to the photocurrent, photodetection measurements were done on bare quartz and c-sapphire substrates. No appreciable photocurrent was recorded on the bare substrates suggesting that the VO$_2$(M1) thin films entirely account for the observed photocurrent.

4. Conclusions

Smooth phase pure VO$_2$(M1) thin films could be deposited on quartz and c-sapphire substrates by two-step DC reactive sputtering. Phase formation and purity were confirmed by XRD and Raman measurements. Morphological analysis by AFM and SEM revealed the nanosized nature of VO$_2$(M1) thin films with a surface roughness of 37 $\pm$ 0.5 nm and 48 $\pm$ 1 nm for VO$_2$-Qu and VO$_2$-Saph thin films respectively, which is smooth enough for various device applications. SMT studies showed an abrupt 1st order transition of the thin films across the transition temperature of 68 °C with a resistance change of 4 and 5 orders of magnitude for VO$_2$-Qu and VO$_2$-Saph thin films respectively which was higher than that reported for VO$_2$(M1) films deposited on a Si(100) substrate[29] by the same technique. The low-cost infrared photodetectors fabricated based on the synthesized VO$_2$(M1) thin films exhibited high IR (λ = 1064 nm and 1550 nm) photoresponse properties. The IR photoresponse of the fabricated devices was dependent on the surface roughness of thin films. Responsivity increased in the order VO$_2$-Qu (14.02 mA W^{-1}) > VO$_2$-Saph (11.12 mA W^{-1}) under an IR (λ = 1064 nm, 250 mW cm^{-2}) laser at a bias voltage of 10 V. An enhanced photoresponse (responsivity of 11.12–14.02 mA W^{-1} and a detectivity of 1.52×10^{12}–1.67×10^{12} jones) was realized with a higher energy (λ = 1064 nm) laser as compared to a lower energy (λ = 1550 nm) laser (responsivity of 3.03–8.65 mA W^{-1} and detectivity of 7.77×10^{11}–1.09×10^{12} jones) attributed to efficient generation of charge carriers at higher laser energy. These results show the suitability of the synthesis technique employed and the substrate choice to prepare VO$_2$(M1) thin films for different applications in optoelectronic and switching devices.

Author contributions

All the authors contributed to the writing of the manuscript. Inyalot Jude Tadeo: (first and corresponding author) carrying out experiments, formal analysis, manuscript writing, review and editing. Saluru B. Krupanidhi: conceptualization, supervision, review and editing. Arun M. Umarji: conceptualization, supervision, formal analysis, review and editing.

Conflicts of interest

There are no conflicts to declare.

Acknowledgements

References

1 W. Li, S. Ji, K. Qian and P. Jin, *J. Colloid Interface Sci.*, 2015, **456**, 166–173.

2 D. Ruzmetov, K. T. Zawilski, S. D. Senanayake, V. Narayanamurti and S. Ramanathan, *J. Phys.: Condens. Matter*, 2008, **20**, 465204.

3 Z. Yang, C. Ko and S. Ramanathan, *Annu. Rev. Mater. Res.*, 2011, **41**, 337–367.

4 C. N. Berglund and H. J. Guggenheim, *Phys. Rev.*, 1969, **185**, 1022–1033.

5 W. W. Li, J. J. Zhu, X. F. Xu, K. Jiang, Z. G. Hu, M. Zhu and J. H. Chu, *J. Appl. Phys.*, 2011, **110**, 1–6.

6 D. P. Zhang, M. D. Zhu, Y. Liu, K. Yang, G. X. Liang, Z. H. Zheng, X. M. Cai and P. Fan, *J. Alloys Compd.*, 2016, **659**, 198–202.

7 C. Wu, F. Feng and Y. Xie, *Chem. Soc. Rev.*, 2013, **42**, 5157–5183.

8 J. Nag and R. F. Haglund, *J. Phys.: Condens. Matter*, 2008, **20**, 264016.

9 Y. Ke, S. Wang, G. Liu, M. Li, T. J. White and Y. Long, *Small*, 2018, **14**, 102025.

10 F. J. Morin, *Phys. Rev. Lett.*, 1959, **3**, 34–36.

11 D. Ruzmetov, D. Heiman, B. B. Claflin, V. Narayanamurti and S. Ramanathan, *Phys. Rev. B: Condens. Matter Mater. Phys.*, 2009, **79**, 10–13.

12 M. Liu, H. Y. Hwang, H. Tao, A. C. Strikwerda, K. Fan, G. R. Keiser, A. J. Sternbach, K. G. West, S. Kittiwatanakul, J. Lu, S. A. Wolf, F. G. Omenetto, X. Zhang, K. A. Nelson and R. D. Averitt, *Nature*, 2012, **487**, 345–348.

13 Z. Zhang, Y. Gao, Z. Chen, J. Du, C. Cao, L. Kang and H. Luo, *Langmuir*, 2010, **26**, 10738–10744.

14 F. Xu, X. Cao, H. Luo and P. Jin, *J. Mater. Chem. C*, 2018, **6**, 1903–1919.

15 Z. Wen, Y. Ke, C. Feng, S. Fang, M. Sun, X. Liu and Y. Long, *Adv. Mater. Interfaces*, 2020, 2001606.

16 J. M. Wu and L. B. Liou, *J. Mater. Chem.*, 2011, **21**, 5499.

17 B. Wang, J. Lai, H. Li, H. Hu and S. Chen, *Infrared Phys. Technol.*, 2013, **57**, 8–13.

18 C. L. Gomez-Heredia, J. A. Ramirez-Rincon, J. Ordonez-Miranda, O. Ares, J. J. Alvarado-Gil, C. Champeaux, F. Dumas-Bouchiat, Y. Ezzahri and K. Joulain, *Sci. Rep.*, 2018, **8**, 1–11.

19 A. Rúa, F. E. Fernández and N. Sepúlveda, *J. Appl. Phys.*, 2010, **107**, 1–5.

20 R. M. Briggs, I. M. Pryce and H. A. Atwater, *Opt. Express*, 2010, **18**, 11192–11201.

21 F. E. F. Horacio Coy, R. Cabrera and N. Sepúlveda, *J. Appl. Phys.*, 2010, **108**, 113115.

22 M. N. Julian, C. Williams, S. Borg, S. Bartram and H. J. Kim, *Optica*, 2020, **7**, 746.

23 F. Zhang, X. Xie, M. Pu, Y. Guo, X. Ma, X. Li, J. Luo, Q. He, H. Yu and X. Luo, *Adv. Mater.*, 2020, **32**, 1908194.

24 A. K. U. Michel, S. Meyer, N. Essing, N. Lassaline, C. R. Lightner, S. Bisig, D. J. Norris and D. N. Chigrin, *Adv. Optical Mater.*, 2021, **9**, 2001243.

25 J. Hou, Z. Wang, Z. Ding, Z. Zhang and J. Zhang, *Sol. Energy Mater. Sol. Cells*, 2018, **176**, 142–149.

26 S. C. H. Woong Choi, M. Yeon Cho, A. Konar, J. Hak Lee and G.-B. Cha, *Adv. Mater.*, 2012, **24**, 5832–5836.

27 Y.-H. Chang, W. Zhang, Y. Zhu, Y. Han, J. Pu, J.-K. Chang, W.-T. Hsu, J.-K. Huang, C.-L. Hsu, M.-H. Chiu, T. Takenobu, H. Li, C.-I. Wu, W.-H. Chang, A. T. S. Wee and L.-J. Li, *ACS Nano*, 2014, **8**, 8582–8590.

28 B. Rajeswaran, I. J. Tadeo and A. M. Umarji, *J. Mater. Chem. C*, 2020, **8**, 12543–12550.

29 I. J. Tadeo, D. Bhardwaj, D. Sheela, S. B. Krupanidhi and A. M. Umarji, *J. Mater. Sci.: Mater. Electron.*, 2020, **31**, 4687–4695.

30 I. J. Tadeo, E. P. Mukhokosi, S. B. Krupanidhi and A. M. Umarji, *RSC Adv.*, 2019, **9**, 9983–9992.

31 I. J. Tadeo, B. Rajeswaran and A. M. Umarji, *J. Phys. D: Appl. Phys.*, 2020, **53**, 185104.

32 J. Jian, X. Wang, L. Li, M. Fan, W. Zhang, J. Huang, Z. Qi and H. Wang, *ACS Appl. Mater. Interfaces*, 2017, **9**, 5319–5327.

33 Y. Ningyi, L. Jinhua and L. Chenglu, *Appl. Surf. Sci.*, 2002, **191**, 176–180.

34 F. Mattelaer, K. Geryl, G. Rampelberg, T. Dobbelaere, J. Dendooven and C. Detavernier, *RSC Adv.*, 2016, **6**, 114658–114665.

35 C. S. Blackman, C. Piccirillo, R. Binions and I. P. Parkin, *Thin Solid Films*, 2009, **517**, 4565–4570.

36 B. W. Mwakikunga, E. Sideras-Haddad and M. Maaza, *Opt. Mater.*, 2007, **29**, 481–487.

37 M. Benkahoul, M. K. Zayed, A. Solieman and S. N. Alamri, *J. Alloys Compd.*, 2017, **704**, 760–768.

38 M. M. Margoni, S. Mathuri, K. Ramamurthi, R. R. Babu and K. Sethuraman, *Thin Solid Films*, 2016, **606**, 51–56.

39 M. Li, S. Ji, J. Pan, H. Wu, L. Zhong, Q. Wang, F. Li and G. Li, *J. Mater. Chem. A*, 2014, **2**, 20470–20473.

40 M. B. Sahana, G. N. Subbanna and S. A. Shivashankar, *J. Appl. Phys.*, 2002, **92**, 6495–6504.

41 P. Schiffer, D. G. Schlom, J. W. Tashman, J. H. Lee, H. Paik, J. A. Moyer, R. Misra, J. A. Mundy and T. Spila, *Appl. Phys. Lett.*, 2015, 063104.

42 J. Zhang, J. Li, P. Chen, F. Rehman, Y. Jiang, M. Cao, Y. Zhao and H. Jin, *Sci. Rep.*, 2016, **6**, 27898.

43 F. Ureña-Begara, A. Crunteanu and J. P. Raskin, *Appl. Surf. Sci.*, 2017, **403**, 717–727.

44 C. Zhang, C. Koughia, Y. Li, X. Cui, F. Ye, S. Shiri, M. Sanayei, S. J. Wen, Q. Yang and S. Kasap, *Appl. Surf. Sci.*, 2018, **440**, 415–420.

45 C. Zhang, C. Koughia, O. Güneş, J. Luo, N. Hossain, Y. Li, X. Cui, S. J. Wen, R. Wong, Q. Yang and S. Kasap, *J. Alloys Compd.*, 2020, **848**, 1–13.

46 S. Ramanathan, *Thin Film Metal-Oxides: Fundamentals and Applications in Electronics and Energy*, Springer, New York, USA, 2010.

47 J. Yoshida, H. Ando and N. Kokubo, *Jpn. J. Appl. Phys.*, 2007, **46**, 738–743.

48 M. Jiang, X. Cao, S. Bao, H. Zhou and P. Jin, *Thin Solid Films*, 2014, **562**, 314–318.

49 M. Ohring, *The Materials Science of Thin Films*, Academic Press, USA, 1992.

50 R. Bharathi, R. Naorem and M. Umarji, *J. Phys. D: Appl. Phys.*, 2015, **48**, 305103.

51 J. Haber, M. Witko and R. Tokarz, *Appl. Catal., A*, 1997, **157**, 3–22.

52 K.-Y. Pan and D.-H. Wei, *Nanomaterials*, 2016, **6**, 140.

53 I. J. Tadeo, R. Parasuraman, S. B. Krupanidhi and A. M. Umarji, *Nano Express*, 2020, **1**, 010005.

54 L. Fan, Y. Chen, Q. Liu, S. Chen, L. Zhu, Q. Meng, B. Wang, Q. Zhang, H. Ren and C. Zou, *ACS Appl. Mater. Interfaces*, 2016, **8**, 32971–32977.

55 R. Baddour-Hadjean, V. Golabkan, J. P. Pereira-Ramos, A. Mantoux and D. Lincot, *J. Raman Spectrosc.*, 2002, **33**, 631–638.

56 M. Castriota, E. Cazzanelli, A. Fasanella and D. Teeters, *Thin Solid Films*, 2014, **553**, 127–131.

57 S. H. Lee, H. M. Cheong, M. J. Seong, P. Liu, C. E. Tracy, A. Mascarenhas, J. R. Pitts and S. K. Deb, *Solid State Ionics*, 2003, **165**, 111–116.

58 Q. Su, C. K. Huang, Y. Wang, Y. C. Fan, B. A. Lu, W. Lan, Y. Y. Wang and X. Q. Liu, *J. Alloys Compd.*, 2009, **475**, 518–523.

59 L. Abello, E. Husson, Y. Repelin and G. Lucazeau, *Spectrochim. Acta*, 1983, **39A**, 641–651.

60 G. I. Petrov, V. V. Yakovlev and J. Squier, *Appl. Phys. Lett.*, 2002, **81**, 1023–1025.

61 C. L. Gomez-Heredia, J. A. Ramirez-Rincon, D. Bhardwaj, P. Rajasekar, I. J. Tadeo, J. L. Cervantes-Lopez, J. Ordonez-Miranda, O. Ares, A. M. Umarji, J. Drevillon,

K. Joulain, Y. Ezzahri and J. J. Alvarado-Gil, *Sci. Rep.*, 2019, **9**, 1–14.

62 C. Chen, R. Wang, L. Shang and C. Guo, *Appl. Phys. Lett.*, 2008, **93**, 2–5.

63 C. A. Schneider, W. S. Rasband and K. W. Eliceiri, *Nat. Methods*, 2012, **9**, 671–675.

64 A. H. J. De Natale and P. J. Hood, *J. Appl. Phys.*, 1989, **66**, 5844–5850.

65 B. D. Gauntt, E. C. Dickey and M. W. Horn, *J. Mater. Res.*, 2009, **24**, 1590–1599.

66 N. Chi-Anh, H. J. Shin, K. Kim, Y. H. Han and S. Moon, *Sens. Actuators, A*, 2005, **123–124**, 87–91.

67 R. Bharathi, R. Naorem and A. M. Umarji, *J. Phys. D: Appl. Phys.*, 2015, **48**, 305103.

68 Z. Yang, S. Hart, C. Ko, A. Yacoby and S. Ramanathan, *J. Appl. Phys.*, 2011, **110**, 033725.

69 Z. Yang, C. Ko and S. Ramanathan, *J. Appl. Phys.*, 2010, **108**, 073708.

70 Z. Jia, J. Xiang, F. Wen, R. Yang, C. Hao and Z. Liu, *ACS Appl. Mater. Interfaces*, 2016, **8**, 4781–4788.

71 E. P. Mukhokosi, S. B. Krupanidhi and K. K. Nanda, *Sci. Rep.*, 2017, **7**, 15215.

72 L. Wang, J. Jie, Z. Shao, Q. Zhang, X. Zhang, Y. Wang, Z. Sun and S. T. Lee, *Adv. Funct. Mater.*, 2015, **25**, 2910–2919.

73 W. Feng, J. Bin Wu, X. Li, W. Zheng, X. Zhou, K. Xiao, W. Cao, B. Yang, J. C. Idrobo, L. Basile, W. Tian, P. H. Tan and P. A. Hu, *J. Mater. Chem. C*, 2015, **3**, 7022–7028.

74 N. Zhong, X. Zhu, Q. Liao, Y. Wang, R. Chen and Y. Sun, *Appl. Opt.*, 2013, **52**, 3937–3945.

75 S. Dias and S. B. Krupanidhi, *Mater. Res. Express*, 2016, **3**, 105006.

76 H. Chang, Z. Sun, M. Saito, Q. Yuan, H. Zhang, J. Li, Z. Wang, T. Fujita, F. Ding, Z. Zheng, F. Yan, H. Wu, M. Chen and Y. Ikuhara, *ACS Nano*, 2013, **7**, 6310–6320.

77 S. Ghosh, B. K. Sarker, A. Chunder, L. Zhai and S. I. Khondaker, *Appl. Phys. Lett.*, 2010, **96**, 163109.

78 S. M. Sze, *Physics of Semiconductor Devices*, John Wiley & Sons, New Jersey, USA, 2nd edn, 1981.

79 J. Yoon, H. Kim, X. Chen, N. Tamura, B. S. Mun, C. Park and H. Ju, *ACS Appl. Mater. Interfaces*, 2016, **8**, 2280–2286.